

Deep ensemble graph neural networks for probabilistic cosmic-ray direction and energy reconstruction in autonomous radio arrays

Arsène Ferrière^{a,b}, Aurélien Benoit-Lévy^a, Olivier Martineau-Huynh^{b,c,d}, Matías Tüeros^e

^aUniversité Paris-Saclay, CEA, List, F-91120 Palaiseau, France

^bSorbonne Université, CNRS, Laboratoire de Physique Nucléaire et des Hautes Énergies (LPNHE), 4 Pl. Jussieu, 75005 Paris, France

^cNational Astronomical Observatories, Chinese Academy of Sciences, Beijing 100101, China

^dSorbonne Université, UPMC Univ. Paris 6 et CNRS, UMR 7095, Institut d'Astrophysique de Paris, 98 bis bd Arago, 75014 Paris, France

^eInstituto de Física La Plata, CONICET - UNLP, Boulevard 120 y 63 (1900), La Plata - Buenos Aires, Argentina

Abstract

Using advanced machine learning techniques, we developed a method for reconstructing precisely the arrival direction and energy of ultra-high-energy cosmic rays from the voltage traces they induced on ground-based radio detector arrays.

In our approach, triggered antennas are represented as a graph structure, which serves as input for a graph neural network (GNN). By incorporating physical knowledge into both the GNN architecture and the input data, we improve the precision and reduce the required size of the training set with respect to a fully data-driven approach. This method achieves an angular resolution of 0.092° and an electromagnetic energy reconstruction resolution of 16.4% on simulated data with realistic noise conditions.

We also employ uncertainty estimation methods to enhance the reliability of our predictions, quantifying the confidence of the GNN's outputs and providing confidence intervals for both direction and energy reconstruction. Finally, we investigate strategies to verify the model's consistency and robustness under real life variations, with the goal of identifying scenarios in which predictions remain reliable despite domain shifts between simulation and reality.

Keywords: ultra-high-energy cosmic rays, radio detection, direction reconstruction, graph neural network, energy reconstruction, deep learning

1. Introduction

When a high-energy cosmic ray enters the Earth's atmosphere, it interacts with air molecules, initiating a cascade of secondary particles. This cascade, known as an extensive air shower (EAS), forms the basis for indirect cosmic ray detection techniques, such as water Cherenkov detectors [1, 2], fluorescence telescopes [3, 4] and in particular radio detectors [5, 6], the technique we will be targeting in this work.

As the EAS propagates through the atmosphere, it produces radio emission through two primary mechanisms [7]: the geomagnetic effect, in which charged particles are deflected by the Lorentz force—perpendicular to both the shower direction and Earth's magnetic field—resulting in linearly polarized radiation in the direction of displacement of the particles; and the charge-excess (or Askaryan) effect, where an excess of electrons at the shower front leads to linearly polarized emission toward the shower axis.

The radio experiment GRAND [8] targets ultra-high-energy neutrinos by autonomously detecting the radio emission from EASs initiated by τ decay products, themselves products of ν_τ interactions with Earth's crust. This requires deployment over vast areas ($O(10^6 \text{ km}^2)$). The current advancement of the experiment targets primarily very inclined ultra-high-energy cosmic

rays (UHECRs), similar to experiments such as AugerPrime [9] and SKA experiment [10].

Precise reconstruction of air-shower parameters is essential for advancing such analyses. Accurate directional reconstruction, for instance, will be mandatory for neutrino astronomy.

To this end, several reconstruction techniques have been developed. Classical likelihood-based methods such as plane wavefront (PWF) fitting [11, 12] can provide good estimates of shower direction. More refined techniques like angular distribution function (ADF) [13] and lateral distribution function (LDF) [14] fitting offer improved reconstruction of both direction and energy from the electric fields recorded by the antennas. However, these approaches can be sensitive to array sparsity and inhomogeneity, threshold effects in station selection, and imperfect calibration, which may introduce biases at large zenith angles or low signal-to-noise ratios. They also rely on empirical models that do not fully capture the underlying physics.

In this work, we introduce a machine learning approach for estimating the direction of the primary particle and the energy deposited in the electromagnetic field, offering robust predictions with associated uncertainty estimates. Our method is hybrid, combining a physics-based estimator with a data-driven model trained on simulations to improve upon the classical PWF problem. Concretely, we compute a first-principles PWF solution and feed residuals (timing residuals with respect to the PWF) to the network together with engineered features (positions, am-

Email address: arsene.ferriere@cea.fr (Arsène Ferrière)

plitudes, peak times), enabling the model to learn systematic corrections while requiring less data to train. The network outputs both point estimates and calibrated uncertainties, capturing aleatoric effects from inherent noise in the data and epistemic variability from model uncertainty due to limited data or model capacity. An early version of this work has been tested on experimental data from the GRAND Collaboration in [15].

The machine learning models employed in this work are Graph Neural Networks (GNNs), in particular edge convolution networks [16] also used in IceCube [17]. GNNs naturally handle variable-size, irregularly spaced antenna layouts and are permutation-invariant by design, making them well suited to autonomous, distributed arrays where the number of triggered antennas and the shape of the footprint can vary widely. GNNs have already shown promising results in related experiments such as ALPAQUITA [18] and IceCube [19], despite differences in experimental configurations, model architectures and reconstruction goal.

To our knowledge, uncertainty quantification in GNN-based reconstruction has only recently begun to be explored in astroparticle physics. Recent work has applied simulation-based inference with a GNN and a normalizing-flow posterior for the reconstruction of ultra-high-energy cosmic-ray directions from radio arrays, achieving calibrated uncertainty estimates [20]. In the neutrino domain, GNNs have been employed for event reconstruction in IceCube with uncertainty quantification [17], although detailed calibration and coverage analyses have not been performed. In this work, we propose a different approach to uncertainty estimation, based on probabilistic regression models and deep ensembles, and perform a quantitative calibration study. This is essential for downstream scientific analyses that rely on reliable confidence regions. The full architecture and uncertainty prediction are summarized in Fig. 4.

We first describe the simulation and signal-conversion pipeline used to generate training and evaluation datasets, including realistic antenna and RF-chain responses and noise modeling. In Section 3, we present the methodology and model architectures, including the physics-informed inputs and uncertainty estimation strategy. In Section 4, we evaluate performance and discuss robustness. We conclude in Section 7.

2. Simulation and Signal Conversion

To train and evaluate the performance of our reconstruction models, we use as input realistic simulations of the voltage signal. To this end, we use ZHAireS Monte Carlo simulations [21], which simulate the development of extensive air showers in the atmosphere, and compute the consequent radio emission propagating through the different layers of the atmosphere. This provides the electric field signal a cosmic ray event would produce at the antenna locations, sampled at 2 GHz for a duration of $4.096 \mu\text{s}$.

Simulations are conducted on a GRAND-like radio antenna array, as shown in Figure 3, following the layout described in [22]. The dataset consists of 25,000 events. Zenith angles θ range from 0° (vertical) to 90° (horizontal) and follow a $-\log(\cos \theta)$ distribution, while azimuth angles ϕ are sampled

uniformly between 0° and 360° . Energies are drawn from a logarithmic distribution between 0.4 and 4 EeV. Shower cores are randomly distributed across the array layout. Half of the events are initiated by proton primaries, and the other half by iron.

To convert these electric field signals into realistic voltage signals, we need a description of a representative antenna response with a realistic noise contribution. The antenna response is computed through a modeling of the effective length, giving the open circuit voltage and the electronics response to convert the open-circuit voltage to measured voltage.

2.1. Efield conversion to voltage

The effective length is a complex 3d vector describing the response of the antenna arms to an electric field. It quantifies both the amplitude sensitivity and phase delay of each antenna arm (X, Y, Z) with ground effects taken into account, depending on the incoming wave direction and frequency ν . It is noted as $\vec{l}_{\text{eff},[X,Y,Z]}(\theta, \phi, \nu)$. This vector can be computed using the NEC4 simulation code [23]. The antenna geometry used for this study is the same antenna geometry as the HorizonAntenna, a butterfly antenna model similar to the ones used by the GRAND collaboration [8]. The direction used to compute the effective length is that of the incoming wave as seen from the antenna position, assuming that the entire radio signal originates from the shower maximum X_{max} .

The open-circuit voltage at frequency ν on arbitrary arm $a \in \{X, Y, Z\}$, $V_{\text{oc},a}(\nu)$ is computed as:

$$V_{\text{oc},a}(\nu) = \vec{l}_{\text{eff},a}(\theta_{\text{max}}, \phi_{\text{max}}, \nu) \cdot \vec{E}(\nu), \quad (1)$$

where $\vec{E}(\nu)$ is the frequency-domain electric field vector at the antenna location. This can be written in matrix form to include all arms by defining the projection operator \mathcal{L} :

$$\mathcal{L} = \begin{pmatrix} \vec{l}_{\text{eff},X} \cdot \mathbf{e}_x & \vec{l}_{\text{eff},X} \cdot \mathbf{e}_y & \vec{l}_{\text{eff},X} \cdot \mathbf{e}_z \\ \vec{l}_{\text{eff},Y} \cdot \mathbf{e}_x & \vec{l}_{\text{eff},Y} \cdot \mathbf{e}_y & \vec{l}_{\text{eff},Y} \cdot \mathbf{e}_z \\ \vec{l}_{\text{eff},Z} \cdot \mathbf{e}_x & \vec{l}_{\text{eff},Z} \cdot \mathbf{e}_y & \vec{l}_{\text{eff},Z} \cdot \mathbf{e}_z \end{pmatrix} \quad (2)$$

and applying it to the electric field vector:

$$\vec{V}_{\text{oc}}(\nu) = \begin{pmatrix} V_{\text{oc},X}(\nu) \\ V_{\text{oc},Y}(\nu) \\ V_{\text{oc},Z}(\nu) \end{pmatrix} = \mathcal{L}(\nu) \cdot \vec{E}(\nu). \quad (3)$$

This formulation allows us to compute, for each antenna and frequency, the expected open-circuit voltage response to an incident electric field, fully accounting for the antenna's directionality and polarization sensitivity. A visualization of the effective lengths used in this study at 60 MHz is shown in Figure 1.

The resulting open-circuit voltage is then passed through a model of the antenna's electronic frequency response composed of the response from every electronic component to obtain the measurable output voltage. In this paper we adopt a frequency-domain transfer function inspired by the GRAND RF-chain response [24, 25] for illustration purposes. This transfer function is approximated from the RF-chain plot in [24] as a smoothed

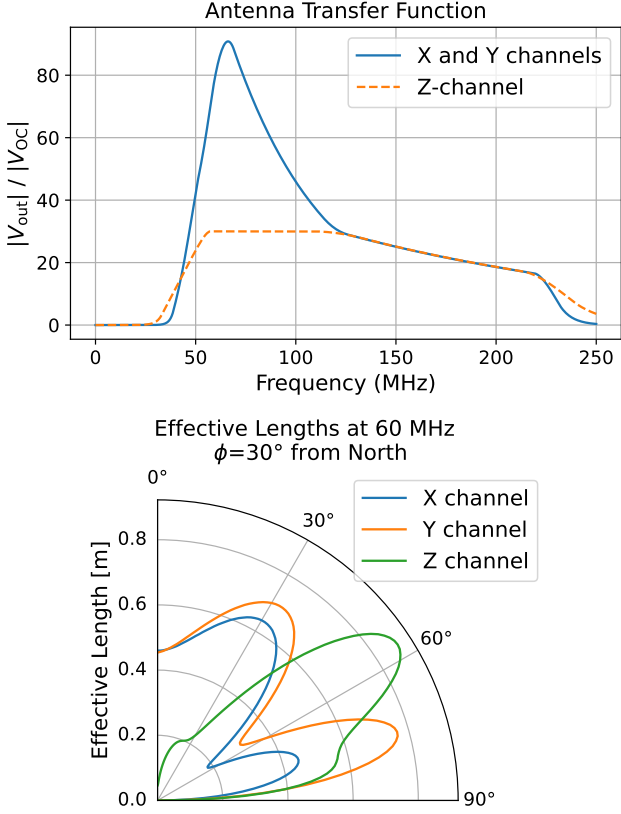


Figure 1: Top: Magnitude of the modeled RF chain transfer function for the X and Y (solid blue) and Z (dashed orange) antenna arms. The magnitude response shows frequency-dependent gain variations. Bottom: Effective lengths of the horizontal antennas at 60 MHz for a signal coming 30° in the presence of ground reflection from north as a function of the zenith angle.

piecewise linear function in logarithmic frequency space. The response is assumed to be identical for the transverse arms (X and Y), while the Z (vertical) arm includes small variations. The phase is modeled as a linearly decreasing function with respect to frequency, which introduces a pure time delay without altering the signal shape. An illustration of the full transfer function is provided in Figure 1.

The effect of the electronics is represented as a diagonal matrix $\mathcal{R}(\nu)$, acting independently on each channel. The final output voltage vector $\vec{V}_{\text{out}}(\nu)$ is then given by:

$$\vec{V}_{\text{out}}(\nu) = \mathcal{R}(\nu) \cdot \vec{V}_{\text{oc}}(\nu) = \mathcal{R}(\nu) \mathcal{L}(\nu) \cdot \vec{E}(\nu). \quad (4)$$

This provides a full simulation of the voltage traces that would be measured by a GRAND-like array of butterfly antennas in response to a cosmic-ray-induced air shower, including realistic modeling of the antenna response and RF chain. However, to make the simulated data suitable for training, it is essential to add noise with a realistic power spectrum and intensity.

2.2. Noise modeling

The total noise added to simulated signals for a realistic modeling comprises three distinct contributions.

- First, we account for time jitter, corresponding to an uncertainty in the time reference associated with the trigger. We model this by applying a 5 ns Gaussian noise to all simulated signals trigger times as performed in [26].
- Second, we consider the galactic noise contribution to the ambient background, dominant part of the noise where the antenna is most sensitive (below 100MHz) [27]. This is treated as an incoherent baseline signal that is added to the trace. The spatial and frequency-dependent galactic brightness temperature $T(\theta, \phi)$ is obtained from LFMMap [28], which provides sky maps in the relevant frequency range. At each point on the sky, the spectral power density per unit solid angle Ω and per frequency ν , $P_{\nu, \Omega}$ can be computed as:

$$P_{\nu, \Omega}(\theta, \phi) = \frac{1}{2} B_{\nu, \Omega}(\theta, \phi) A_{\text{eff}}(\theta, \phi), \quad (5)$$

$$B_{\nu, \Omega}(\theta, \phi) = \frac{2\nu^2 k_B T(\theta, \phi)}{c^2}. \quad (6)$$

where $A_{\text{eff}}(\theta, \phi) = \|\vec{l}_{\text{eff}, i}\|^2$ is the effective area of antenna arm i , which depends on the direction (θ, ϕ) as seen from the antenna location and thus on the local sidereal time. $B_{\nu, \Omega}$ is the spectral radiance, representing the received power per frequency, per unit area, and per solid angle. The factor $\frac{1}{2}$ in equation 5 results from the fact that the emission is not polarized, thus only half of the power aligns with \vec{l}_{eff} . An illustration of the effective area of the X arm and the spectral radiance $B_{\nu, \Omega}$ is shown in Figure 2.

Integrating this power over the full sky yields the total spectral power P_ν received at each frequency. This power corresponds to an open-circuit voltage spectral density on the antenna given by:

$$V_{\text{OC, RMS}}^2(\nu) = \frac{P_\nu}{Z_0}, \quad (7)$$

where Z_0 is the impedance of free space. The contribution is then filtered through the RF chain response (as previously modeled) to obtain the output root-mean-square voltage per frequency unit:

$$V_{\text{RMS}}^2(\nu) = |\mathcal{R}(\nu)|^2 \cdot V_{\text{OC, RMS}}^2(\nu). \quad (8)$$

To generate time-domain noise traces, we construct the Fourier transform of a random signal with magnitude sampled from a Gaussian distribution with standard deviation

$$V_{\text{out}} = \sqrt{\frac{N f_s}{2}} \cdot V_{\text{RMS}}, \quad (9)$$

where N is the number of time samples and f_s the sampling frequency. The phase at each frequency is drawn uniformly at random between 0 and 2π .

We neglect radio-frequency interference (RFI), assuming that digital mitigation techniques, such as notch filtering, are applied to suppress contaminated frequency bands.

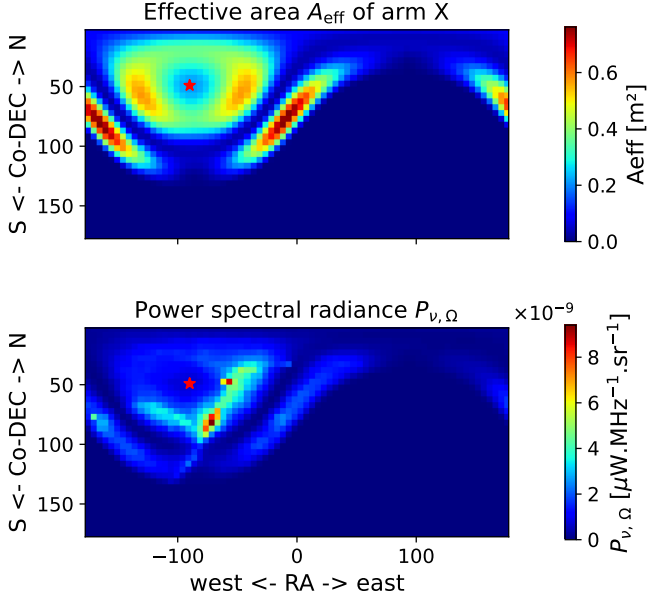


Figure 2: Effective area (A_{eff}) and power spectral density (P_ν) for arm X of the detector at 60 MHz. The top panel shows the effective area as a function of right ascension (RA) and latitude. The bottom panel displays the power spectral radiance map, derived from the temperature map and effective area, also as a function of RA and latitude. The red star indicates the zenith at detector's location. Both plots correspond to a local sidereal time of 18:00.

- Finally, we account for antenna calibration uncertainties by introducing a multiplicative smearing factor. This is implemented by multiplying each noisy signal by a random coefficient sampled from a Gaussian distribution centered at 1 with a standard deviation of 7.5%. This mimics the typical uncertainty on antenna calibration observed in real systems.

To emulate realistic triggering conditions, we apply a quality cut. Antennas with low signal amplitudes would not trigger in practice, so we discard any antenna signal whose peak amplitude is below $5\sigma_{\text{noise}}$, with σ_{noise} the standard deviation of the noise, of around 1.0 mV at RFchain output with the antenna model used. This cut ensures that only realistic detections are retained and that the extracted peak values are not dominated by noise fluctuations. Additionally, if too few antennas are triggered, the coincidence detection would not trigger and the event would not be recorded [27]. We thus keep only events with more than five antennas remaining after the quality cut.

In total, 7975 simulated events are retained from an initial set of 25,000. The median number of antennas triggered per event after the cuts is 20.

3. Graph neural network on distributed radio antenna arrays

3.1. Motivations for using graph neural networks

Radio antenna arrays used to detect ultra-high-energy cosmic rays (UHECRs) are usually made up of many autonomous stations spread over large areas. When an extensive air shower

(EAS) occurs, it triggers a subset of these antennas, which can vary significantly in number and spatial distribution depending on the shower's energy, direction, and core location. This variability presents several challenges for traditional machine learning models:

- **Variable Input Size:** The number of triggered antennas can differ widely from event to event, making it difficult to use models that require fixed-size inputs, such as fully connected neural networks or convolutional neural networks (CNNs).
- **Irregular Spatial Distribution:** The triggered antennas are not arranged in a regular grid but are instead scattered with some irregularities. This irregularity complicates the application of CNNs, which rely on regular patterns.
- **Permutation Invariance:** The order in which antenna data is presented should not affect the model's predictions. Traditional models may inadvertently learn to depend on the input order, leading to inconsistent results.

Graph Neural Networks (GNNs) [29] are designed to address these challenges effectively. GNNs operate on graph-structured data, where nodes represent entities (in this case, antennas) and edges represent relationships or connections between them (in this case, spatial proximity).

3.2. Analytical reconstruction from the wavefront

The machine-learning approach considered in this paper uses a first estimate of the direction to improve the reconstruction. This information must be fast to compute and sufficiently accurate. For this purpose, we assume a planar wavefront for the radio signal and use the semi-analytical solver described in [11]. Under this assumption, the signal arrival times are linearly related to the antenna positions:

$$\mathbf{T} = \frac{1}{c'} \mathbf{P} \mathbf{k} + \boldsymbol{\epsilon}, \quad (10)$$

where \mathbf{T} is the zero-mean vector of arrival times, and \mathbf{P} is the matrix of antenna positions. c' is the average speed of light in the atmosphere. The vector $\boldsymbol{\epsilon}$ represents timing noise, accounting for time jitter. The unit vector $\mathbf{k} \in \mathbb{R}^3$ is the propagation direction of the planar wavefront, which is the quantity to be reconstructed.

The propagation vector is obtained by solving the following constrained optimization problem:

$$\mathbf{k}_{\text{PWF}} = \arg \min_{\mathbf{k}} \mathbf{k}^T \mathbf{A} \mathbf{k} - 2\mathbf{b}^T \mathbf{k}, \quad s.t. \quad \|\mathbf{k}\| = 1. \quad (11)$$

It can be solved analytically provided an assumption of a flat layout or semi-analytically for an exact solution with a single variable convex optimization scheme. Both methods are described in [11].

From this reconstruction, we define the PWF arrival times as:

$$\mathbf{T}_{\text{PWF}} = \frac{1}{c'} \mathbf{P} \mathbf{k}_{\text{PWF}} \quad (12)$$

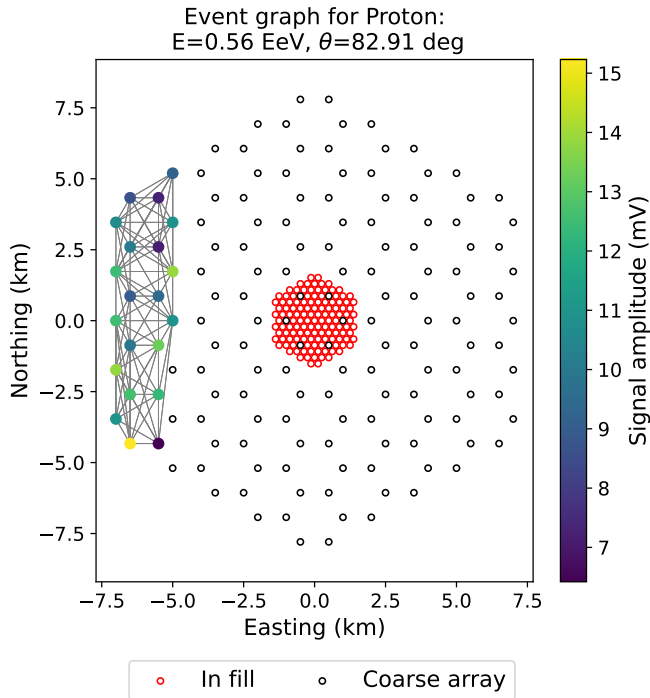


Figure 3: Example of a graph constructed from a simulated event. Triggered antennas are represented as nodes (blue dots), with edges (gray lines) connecting each antenna to its eight nearest neighbors. The color of each node corresponds to the signal amplitude recorded at that antenna, illustrating the spatial distribution of the detected signals across the array.

and PWF residual timings as:

$$\Delta_{\text{PWF}} = \mathbf{T} - \mathbf{T}_{\text{PWF}} \quad (13)$$

Both the reconstructed direction \mathbf{k}_{PWF} and the residuals Δ_{PWF} are provided to the GNN as inputs for an initial estimate of the target direction.

3.3. Preprocessing for GNN input

To construct data suitable for GNN input, we follow a systematic preprocessing pipeline. For every simulated event, a graph structure is generated by connecting each triggered antenna to its eight nearest neighbors. This configuration was found to optimize model precision: fewer neighbors reduce connectivity, while more neighbors do not yield significant precision improvements and worsen compute performance. With eight neighbors per node and the number of graph layers used in the model (see the next section), information is propagated across the entire graph, which may explain why increasing the connectivity does not improve performance. An example of such a graph is shown in Fig. 3.

To every node is associated a set of features, which we call input features. These features can be explicitly derived:

1. The **3D position** of the antenna, $(\mathbf{X}, \mathbf{Y}, \mathbf{Z})$, which is known precisely from the array layout. The X axis is pointing toward the geomagnetic north, Y toward the west and Z upward.
2. The **time of arrival** of the radio signal, \mathbf{T} , at each antenna. This is what allows us to describe the wavefront shape and thus to estimate the direction of the shower. This quantity, along with the position of the antenna, is used in classical methods such as the PWF fit method to estimate the direction or the spherical wavefront (SWF) fit method to estimate a point source position, which is a proxy for the X_{max} position. The GNN will thus be given this information as input.
3. The **signal amplitudes**, \mathbf{A} , are also extracted and used as input, as they contain information on the Cherenkov compression effect—where, for observers at a specific angle, contributions from different parts of the shower arrive coherently and enhance the signal amplitude—and thus encode information about the shower geometry. It is, for instance, used in ADF [13] as a way to aim the shower axis once a proxy for X_{max} is known. Finer details of the amplitude distribution, like early-late asymmetry or charge-excess asymmetry, can in principle refine the direction reconstruction [13] and can be picked out by the machine learning models.
4. The **residual of the PWF timings** Δ_{PWF} , computed from the analytical PWF reconstruction from [11]. It is finer information about the wavefront shape; it represents the deviation of the wavefront from a plane.

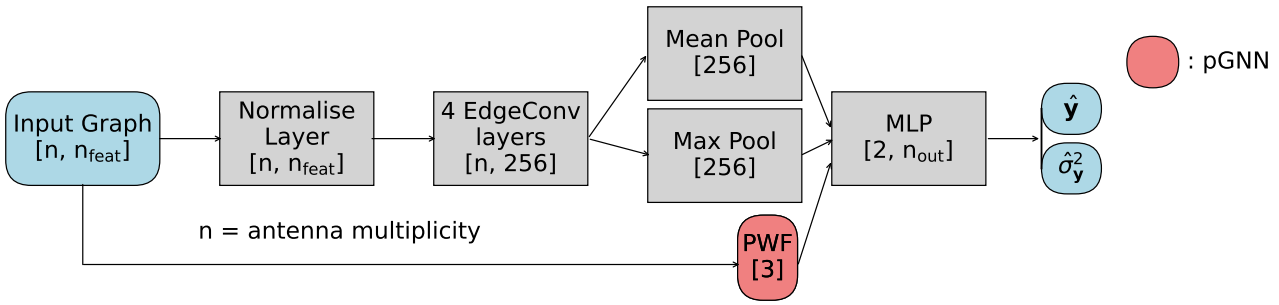
To extract the time of arrival and the amplitude, we disregard the upward component of the electric field, as in practice this polarization is noisier due to RFI and EAS emissions are predominantly in the horizontal components at the simulations location. We then compute the Hilbert envelope of the discretized voltage signal on the two transverse components (X: South-North, Y: East-West). The time of arrival is defined as the time of the maximum of this envelope, and the amplitude as its value at this time. For every event, we also save, the three coordinates of the direction vector obtained by the PWF fit, which will be used as features after the graph stage.

3.4. Architecture

In the rest of the paper, we will mostly consider one model architecture, called pGNN, where the output from a physics based estimator (here the PWF) is used as input to the GNN. In this case, the three coordinates of the PWF reconstructed vector are given as global features, and the timing residuals with respect to the PWF are given as input features for every node. This allows the model to learn systematic corrections to the PWF reconstruction, which is a first-order approximation of the wavefront shape.

We will also consider the fully data-driven version of the model, called rGNN (for raw-GNN) as a comparison point for some tests. It means that it only uses features obtained directly from the voltage signals, without any physics-based reconstruction (only time and amplitude of the peak voltage).

The normalizing layer forces derived inputs to be distributed with comparable statistics, typically close to a centered and normalized Gaussian. This helps the model to converge faster



Model	Node features	n_{feat}	Global features
rGNN	Positions + times + amplitudes	5	No
pGNN	Positions + times + amplitudes + PWF residuals	6	PWF direction

Figure 4: Illustration of the different architectures used in this study. The main gray branch represents the rGNNs, which rely solely on explicitly derived features in a data-driven approach. The inclusion of the red PWF branch describes the pGNN models, where physics-based inputs are integrated to enhance precision. In this architecture, the difference between the measured timings and the expected timings from the PWF model is added as a graph input feature which increases n_{feat} from 5 to 6.

and avoid some numerical issues. For every feature, we compute a transformation to map the distribution to a Gaussian-like distribution.

The EdgeConv layers, as described in [16], compute, for every connected pair of nodes, a non-linear parametrizable function of their features as follows:

$$x_i^{(k+1)} = \frac{1}{|\mathcal{N}_i|} \sum_{j \in \mathcal{N}_i} f_p^{k+1}(x_i^{(k)}, x_j^{(k)}), \quad (14)$$

with \mathcal{N}_i the neighbors of node i , $x_i^{(k)}$ the features of node i after layer k , and f_p^{k+1} a parametrizable function with parameters p . In our case, it is a 2-layer multilayer perceptron (MLP), i.e., a fully connected feedforward neural network. We use four such EdgeConv layers.

To flatten into a vector, we use max-pooling and mean-pooling layers. For every feature, we keep the maximum (respectively mean) value across nodes and concatenate them into a vector, used as input to an MLP that predicts the output quantities. For every reconstructed quantities, models predict two values: a mean that will be the model reconstructed value and a variance to quantify uncertainty around the mean value by assuming that the errors made by the model are Gaussian. This is imposed during training as described in the next paragraph.

Finally, for every reconstruction task, we train an ensemble of N models with different weight initializations to improve uncertainty estimation and prediction accuracy.

3.5. Training and inference procedure

We train an ensemble of 12 models, which was found sufficient to improve robustness and reduce prediction variance, as no further gains in precision or uncertainty calibration are observed for larger ensemble sizes. The models differ only in their initial weights and training data ordering. To train the model, we need to define a loss function. As we want to predict both a point estimate and an uncertainty, we use a Gaussian negative log-likelihood [30] (NLL) loss function, which encourages

well-calibrated predictive distributions and penalizes both biased means and incorrect variance estimates. It is defined for a scalar target y as:

$$\mathcal{L}(\hat{y}, \hat{\sigma}^2) = \frac{1}{2} \left(\frac{(y - \hat{y})^2}{\hat{\sigma}^2 + \epsilon} + \log \hat{\sigma}^2 \right), \quad (15)$$

where \hat{y} is the predicted mean and $\hat{\sigma}$ the predicted standard deviation for the target y . A small value ϵ is added to the variance term for numerical stability (here 10^{-6}). This loss function, a generalization of the classical mean squared error (MSE) loss, encourages the model to produce accurate point estimates while also providing well-calibrated uncertainty estimates.

Direction reconstruction

For direction reconstruction, we predict the three Cartesian components of the unit direction vector $\mathbf{k} = (k_x, k_y, k_z)$ defined from the zenith angle θ and azimuth angle ϕ as:

$$\mathbf{k} = - \begin{pmatrix} \sin \theta \cos \phi \\ \sin \theta \sin \phi \\ \cos \theta \end{pmatrix}. \quad (16)$$

This description is convenient for training the GNN for direction reconstruction, as it avoids singularities at the zenith and allows for straightforward computation of angular differences. It also facilitates the use of loss functions based on Euclidean distances. The predicted zenith and azimuth angles can be derived from these components by inverting equation 16.

The loss function for direction reconstruction is then defined as the sum of the NLL losses for each component of the direction vector:

$$\mathcal{L} = \frac{1}{2} \sum_{c \in \{x, y, z\}} \left(\frac{(k_c - \hat{k}_c)^2}{\hat{\sigma}_c^2 + \epsilon} + \log \hat{\sigma}_c^2 \right), \quad (17)$$

where k_c are the true components of the direction vector, \hat{k}_c are the predicted components, and $\hat{\sigma}_{k_c}$ are the predicted uncertainties for each component.

This function does not consider the unit norm constraint of \mathbf{k} , which is addressed during inference by normalizing the predicted vector. However, it does not significantly impact the training process as the model learns to predict values close to the unit sphere. Other loss functions have been tested. In particular, the MSE loss function was considered; it yielded similar results for reconstruction precision but did not provide calibrated uncertainty estimates, even using ensemble methods.

Energy reconstruction

For energy reconstruction, the Gaussian-NLL loss function applied to the log energy was chosen as it naturally handles the wide dynamic range of energies. The loss function for energy reconstruction is given by equation 15 where y stands for $\log E$ E being the true electromagnetic energy of the shower.

Each model is trained using the Adam optimizer with adaptive learning rates to ensure efficient convergence. A batch size of 4 is used for training. The dataset is split into 5000 events for training and 1200 events for validation. All models are trained on the same set of events. This split remains identical for all models to ensure comparability; only the initial weights and the input data order are modified. Training is conducted for a maximum of 120 epoch which always lead to convergence of the models. Early stopping was also considered to stop the training if no improvement is observed in the validation loss over a predefined number of epochs.

Each model f_i (where $i = 1, 2, \dots, 12$) is trained independently for predicting the best estimate \hat{y}_i and its associated uncertainty $\hat{\sigma}_{y,i}$ for a given quantity. The ensemble prediction \hat{y} is computed as the mean of the individual model predictions:

$$\hat{y} = \frac{1}{N} \sum_{i=1}^N \hat{y}_i,$$

where $N = 12$ is the number of models in the ensemble.

The associated uncertainty $\hat{\sigma}_y$ is estimated by combining the predicted uncertainties $\hat{\sigma}_{y,i}$ from each model and the variance of the predictions:

$$\hat{\sigma}_y^2 = \frac{1}{N} \sum_{i=1}^N \hat{\sigma}_{y,i}^2 + \frac{1}{N} \sum_{i=1}^N (\hat{y}_i - \hat{y})^2. \quad (18)$$

This formulation captures both aleatoric uncertainty through the individual model uncertainties combined (left term) and epistemic uncertainty (model uncertainty due to limited data or model capacity) through the variance of the ensemble predictions (right term).

4. Performances

Before evaluating the performance of the models, we first assess their convergence during training. We then present the results for direction and energy reconstruction, focusing first on accuracy. We will assess the uncertainty estimation and calibration in the next section.

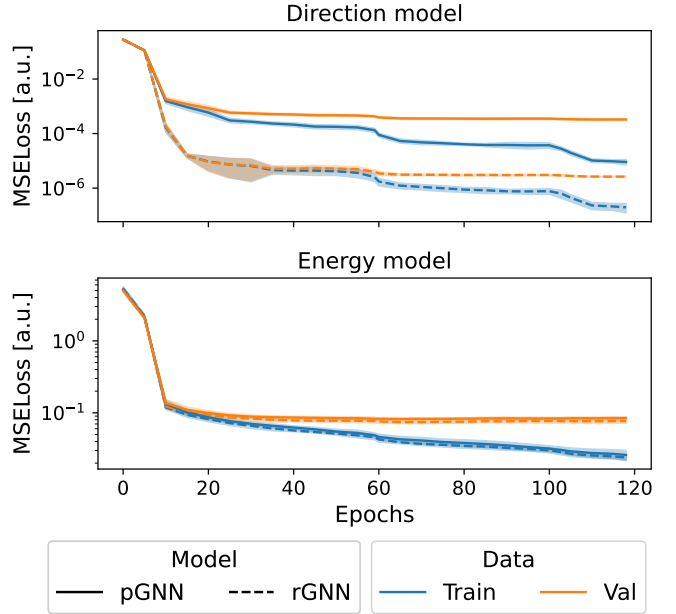


Figure 5: Evolution of the MSE loss on the training set and validation set over epochs for the 12 ensemble members of rGNN and pGNN for energy and direction reconstruction. The introduction of the PWF information significantly decreases the training and validation mean square error.

4.1. Model convergence

To evaluate model convergence, we focus on the evolution mean squared error of the models on the training and validation set over epochs during training.

To assess training stability and potential overfitting, we monitored the error across the 12 ensemble members on Figure 5. The mean square error is represented across training on the training set (blue) and validation set (orange), the transparent envelopes represent the standard deviation over all 12 models. All runs converged smoothly (no loss evolution for more than 20 epochs), to the same values for both validation and training. We do that the validation errors stabilize early on in the training while the performance on training set keeps improving. On all training curves, we observe steps of rapid decrease followed by plateaus. This is due to the learning rate scheduler, which reduces the learning rate when no improvement is observed on the validation loss. We also notice that the introduction of the PWF information significantly decreases the training and validation losses for direction reconstruction. For energy reconstruction, the PWF information doesn't affect the evolution of the MSE error.

We also probed data efficiency by training with subsampled datasets (25%, 50%, 75% of the available training set). All configurations converged, with performance degradation at smaller sizes. For direction reconstruction, models that include physics-informed inputs (PWF residuals) were the most sample-efficient, reaching better performance with fewer events, while purely data-driven variants benefited more from the full dataset but never reached the same precision. This highlights the value of incorporating domain knowledge to guide learning, especially in data-scarce regimes (see Appendix A). This effect is less pro-

nounced for energy reconstruction as the physical knowledge given to the model is not directly a proxy of the energy.

4.2. Direction reconstruction performances

Constructing the ensemble model as described in Section 3.5 yields a robust direction estimator with associated uncertainties. We define the angular resolution as the median angular error between the true and reconstructed directions, where the angular error is defined as:

$$\Psi = \arccos(\mathbf{k} \cdot \hat{\mathbf{k}}). \quad (19)$$

We show in Figure 7 the distribution of angular errors for single models, the ensemble mean prediction, and the PWF baseline. For pGNN models, the ensemble mean attains a median angular error of 0.092° , clearly outperforming both single models (0.11°) and the PWF baseline (0.16°), demonstrating the variance reduction and accuracy gains from ensembling. For rGNN models, the ensemble mean reaches 0.66° , better than single models (0.86°) but not as precise as PWF. Its distribution is not represented, as its width exceeds those of the PWF and pGNN models by more than an order of magnitude, rendering a joint visualization impractical. This highlights the benefit of physics-informed inputs. Even without them, the ensemble still provides a fully orthogonal alternative to PWF. The azimuth reconstruction performs better than PWF, but this is primarily because the zenith reconstruction has improved. The prediction is biased in θ but by a value an order of magnitude lower than the variance of the error.

The angular resolution strongly depends on the number of triggered antennas: with fewer stations, less timing/geometric information and a shorter lever arm are available. This is illustrated in Figure 8 for the residual on θ , which dominates the total angular error. Since multiplicity correlates with energy and zenith, the resolution also varies with these parameters, but less significantly. For very inclined showers, footprints are larger and more antennas trigger, yet the θ resolution degrades at the highest zeniths due to the reduced vertical lever arm. No significant bias is observed in any regime, making the pGNN predictions trustworthy.

The distance of the shower core to the array center affects the PWF angular resolution significantly (see 6) as events landing far from the array center only show one side of the spherical wavefront, inducing a bias in the best fit plane. This bias is corrected by the pGNN, which shows a stable angular resolution across core distances. Overall, the ensemble pGNN model achieves robust performance across a wide range of event characteristics, demonstrating its effectiveness for direction reconstruction in radio antenna arrays.

4.3. Performances on energy reconstruction

As the reconstructed quantity for energy is the logarithm of the energy, the ensemble prediction is the mean of the predicted log energies; in other words, the predicted energy is the geometric mean of the individual model predictions:

$$\hat{E} = \exp\left(\frac{1}{N} \sum_{i=1}^N \log \hat{E}_i\right) = \left(\prod_{i=1}^N \hat{E}_i\right)^{\frac{1}{N}}. \quad (20)$$

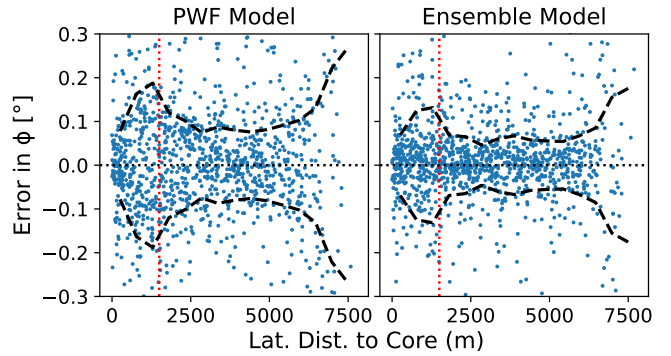


Figure 6: Azimuth-angle residual ($\Delta\phi$) versus core distance to the array center for the ensemble pGNN and the PWF estimator. The PWF estimator (orange) shows a significant bias for events landing far from the array center, while the pGNN (blue) maintains a stable resolution without bias across core distances. The shaded band indicates the central 68% interval.

The energy reconstruction performance is evaluated using the relative error between the true and reconstructed energies:

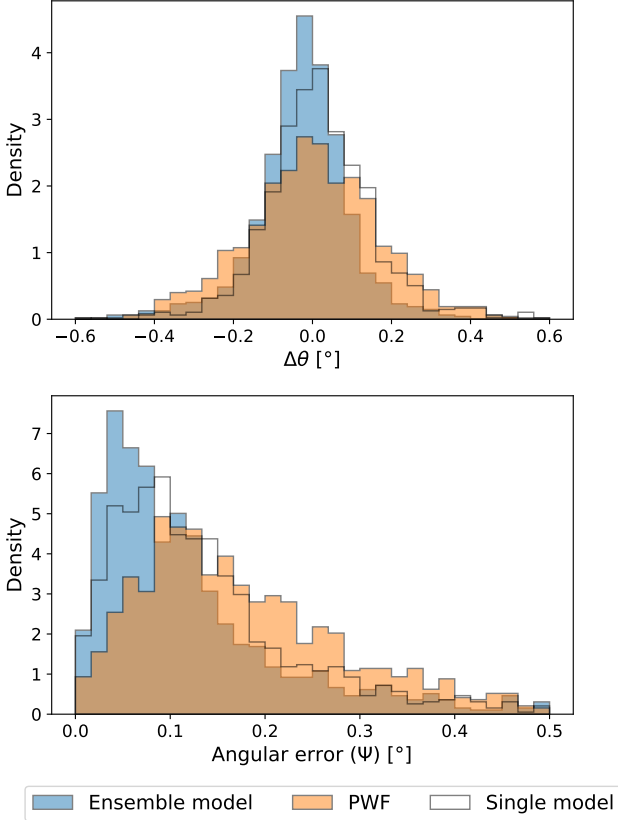
$$\frac{\Delta E}{E} = \frac{E - \hat{E}}{E}. \quad (21)$$

The energy resolution is defined as the 68% centered quantile of the distribution of the relative error:

$$\begin{aligned} \text{Energy resolution} &= \frac{1}{2} \left(Q_{84\%} \left(\frac{\Delta E}{E} \right) - Q_{16\%} \left(\frac{\Delta E}{E} \right) \right) \\ &= Q_{68\%} \left(\left| \frac{\Delta E}{E} \right| \right). \end{aligned} \quad (22)$$

Figure 9 shows the distribution of relative errors for single models and for the ensemble mean prediction. The ensemble mean achieves an energy resolution of 16.4%, better than single models (19.5%). The single models tend to have outliers with large errors, outside of the range shown in the histogram. In the ensemble model, these errors are averaged out. We also see a small bias when separating events by primary type. In particular, iron primaries have their energy slightly underestimated, while proton primaries are slightly overestimated. This is likely due to differences in shower development and radio emission characteristics between the two primary types, which are not fully captured by the model. However, the bias remains small, and the overall energy resolution is robust across primary types.

The sensitivity of the energy resolution to various event parameters is illustrated in Figure 10. The energy resolution improves with the number of antennas triggered; below 10 antennas triggered, the resolution is 21%, above, it improves to 16%. The resolution is more steady with zenith angle, but a bias is observed at high zenith where the energy tends to be underestimated. This effect is more pronounced when looking at the X_{\max} distance to the array, where events with X_{\max} far from the array. This is in fact the same phenomenon, as more inclined events cross a larger distance in the atmosphere and thus reach X_{\max} further away. This is most likely because when showers develop high in the atmosphere, the geomagnetic emissions lose coherence [31], thus the electromagnetic emission is weaker and the energy is underestimated. An important aspect is that the resolution is very stable across the energy range considered,



Method	$\langle \Delta\theta \rangle [^\circ]$	$\sigma_{\Delta\theta} [^\circ]$	$q_{50,\Psi} [^\circ]$	$q_{95,\Psi} [^\circ]$
PWF	5.8×10^{-4}	1.9×10^{-1}	1.6×10^{-1}	4.5×10^{-1}
Single pGNN	2.8×10^{-2}	1.5×10^{-1}	1.1×10^{-1}	4.1×10^{-1}
Ens. pGNN	-2.8×10^{-2}	1.4×10^{-1}	9.2×10^{-2}	3.8×10^{-1}
Single rGNN	8.6×10^{-2}	9.7×10^{-1}	8.6×10^{-1}	3.5×10^0
Ens. rGNN	-8.8×10^{-2}	9.0×10^{-1}	6.6×10^{-1}	3.1×10^0

Figure 7: Distribution of angular errors for single pGNN models, the ensemble mean prediction, and the PWF estimator. The ensemble pGNN (blue) achieves a mean angular error of 0.092° , significantly outperforming both single models (gray) (0.12°) and the PWF baseline (orange) (0.18°). The table summarizes the performances of all models considered. The quantities shown are the mean error on zenith angle, the standard deviation of the error on zenith angle, the mean angular error, and the 95th percentile of the angular error distribution.

demonstrating the model’s ability to handle the wide dynamic range of cosmic ray energies. The distance of the shower core to the array center has a small impact on the energy resolution, with slightly better performance for events landing closer to the center where the antenna density is higher. Overall, the ensemble pGNN model achieves robust energy reconstruction performance across a wide range of event characteristics.

5. Uncertainty estimation and calibration

In addition to predicting direction and electromagnetic energy, it is crucial to provide reliable uncertainty estimates for these predictions. To achieve this, we modeled the prediction errors on the reconstructed quantity as following a Gaussian distribution and trained multiple models using a Gaussian negative log-likelihood loss function. Details are given in Section 3.5.

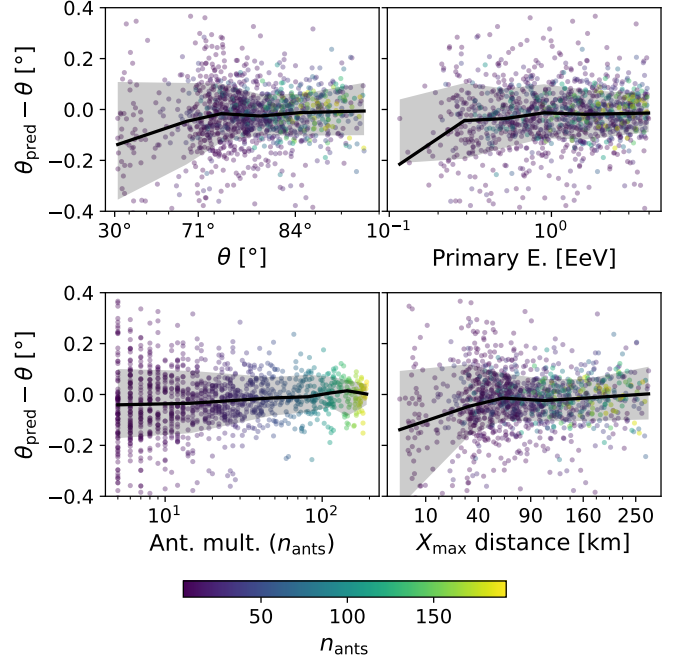


Figure 8: Zenith-angle residual ($\Delta\theta$) versus event parameters for the ensemble pGNN. Top-left: zenith; top-right: primary energy; bottom-left: triggered-antenna multiplicity; bottom-right: core distance to the array center. Performance depends mainly on multiplicity; no significant bias is observed. The shaded band indicates the central 68% interval.

This allows for better interpretation of the results and for the construction of confidence regions for the reconstructed quantities. Such reconstruction can be seen on Fig. 11. Here, the targeted quantity is the direction, represented by a red cross. We see that the individual models, green dots, improve the PWF reconstruction in blue and define the ensemble prediction as a green cross, the confidence interval can be represented around the prediction from the deep ensemble variance prediction.

5.1. Uncertainty calibration and propagation

The direction models predict the Cartesian components of the unit vector $\hat{\mathbf{k}}$ together with per-component standard deviations $\hat{\sigma}_x, \hat{\sigma}_y, \hat{\sigma}_z$. We form the (diagonal) covariance

$$\hat{\Sigma}_{ij} = \hat{\sigma}_i^2 \delta_{ij}, \quad i, j \in \{x, y, z\}. \quad (23)$$

Because the physical direction lies on the unit sphere, we project this unconstrained Gaussian onto the tangent plane at $\hat{\mathbf{k}}$. Using the Gaussian conditioning formula for the linear constraint $\hat{\mathbf{k}}^T (\mathbf{k} - \hat{\mathbf{k}}) = 0$, the constrained covariance is

$$\hat{\Sigma}_\perp = \hat{\Sigma} - \frac{\hat{\Sigma} \hat{\mathbf{k}} \hat{\mathbf{k}}^T \hat{\Sigma}}{\hat{\mathbf{k}}^T \hat{\Sigma} \hat{\mathbf{k}}}. \quad (24)$$

We then propagate uncertainties to the spherical angles (θ, ϕ). Two equivalent routes can be used.

1. Direct Jacobian from Cartesian to angles (valid away from

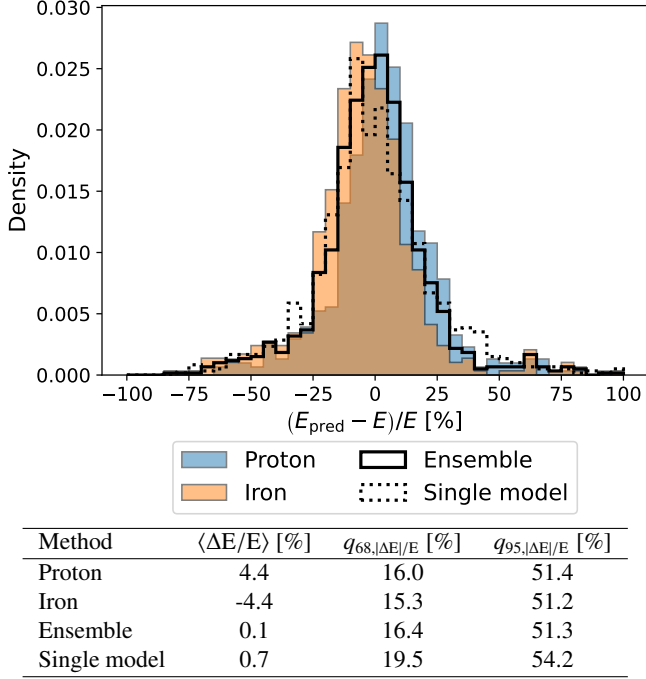


Figure 9: Distribution of relative energy errors $(E_{\text{pred}} - E)/E$. Blue and orange filled histograms: ensemble pGNN predictions for proton and iron primaries, respectively. Bold solid line: ensemble distribution; dotted line: single model distribution. The ensemble pGNN achieves an energy resolution of 16.4% (68% quantile of the absolute relative residuals), compared with 19.5% for single models. A small bias is visible in the ensemble: iron events are slightly underestimated while proton events are slightly overestimated, but resolution is the same.

the poles, $\sin \theta \neq 0$):

$$J = \begin{pmatrix} \frac{\partial \theta}{\partial k_x} & \frac{\partial \theta}{\partial k_y} & \frac{\partial \theta}{\partial k_z} \\ \frac{\partial \phi}{\partial k_x} & \frac{\partial \phi}{\partial k_y} & \frac{\partial \phi}{\partial k_z} \\ \frac{\partial \theta}{\partial k_x} & \frac{\partial \theta}{\partial k_y} & \frac{\partial \theta}{\partial k_z} \end{pmatrix} \quad (25)$$

$$= \begin{pmatrix} 0 & 0 & \frac{1}{\sin \theta} \\ \frac{\sin \phi}{\sin \theta} & -\frac{\cos \phi}{\sin \theta} & 0 \end{pmatrix}, \quad (26)$$

$$\hat{\Sigma}_{\theta,\phi} = J \hat{\Sigma}_{\perp} J^T. \quad (27)$$

- Using the Schur complement inversion method, the previous expression is equivalent to the following, which is numerically more robust near the poles:

$$\hat{\Sigma}_{\theta,\phi} = [\mathbf{R}_a^T \hat{\Sigma}^{-1} \mathbf{R}_a]^{-1}, \quad (28)$$

with the Jacobian from angles to Cartesian (using Eq. 16):

$$\mathbf{R}_a = \begin{pmatrix} \frac{\partial k_x}{\partial \theta} & \frac{\partial k_x}{\partial \phi} \\ \frac{\partial k_y}{\partial \theta} & \frac{\partial k_y}{\partial \phi} \\ \frac{\partial k_z}{\partial \theta} & \frac{\partial k_z}{\partial \phi} \end{pmatrix} = \begin{pmatrix} -\cos \theta \cos \phi & \sin \theta \sin \phi \\ -\cos \theta \sin \phi & -\sin \theta \cos \phi \\ \sin \theta & 0 \end{pmatrix}. \quad (29)$$

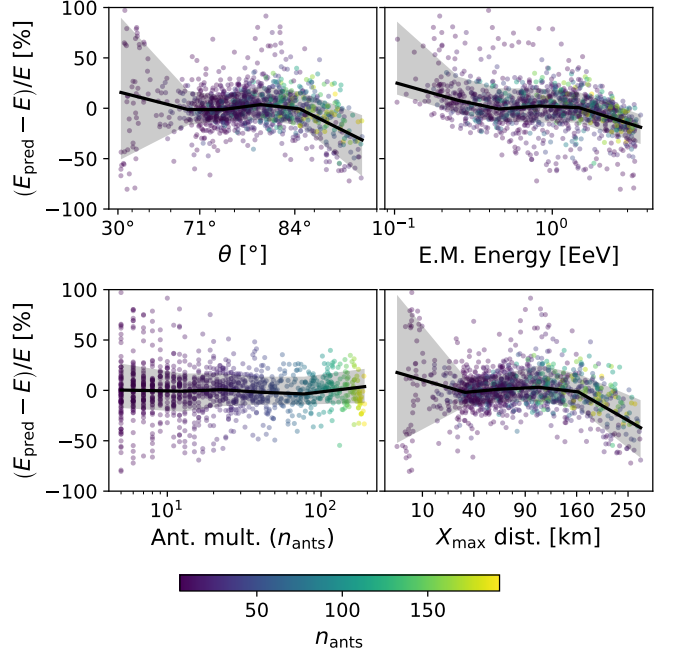


Figure 10: Relative energy error as a function of event parameters for the ensemble pGNN. Top-left: zenith angle; top-right: electromagnetic energy; bottom-left: number of triggered antennas; bottom-right: distance from X_{max} to the array. Blue points denote individual events; the black curve shows the bin-wise mean with a shaded 68% envelope, representing the energy resolution as a function of the horizontal axis. Bias is observed at high zenith angles corresponding to large distances of the emission point.

From $\hat{\Sigma}_{\theta,\phi}$ we extract

$$\hat{\sigma}_{\theta} = \sqrt{(\hat{\Sigma}_{\theta,\phi})_{11}}, \quad \hat{\sigma}_{\phi} = \sqrt{(\hat{\Sigma}_{\theta,\phi})_{22}}, \quad \hat{\rho}_{\theta,\phi} = \frac{(\hat{\Sigma}_{\theta,\phi})_{12}}{\hat{\sigma}_{\theta} \hat{\sigma}_{\phi}}. \quad (30)$$

This projection removes the non-physical radial component and yields calibrated uncertainties in (θ, ϕ) . In practice, we use Eq. 28 for its simplicity. All propagations above rely on first-order (local) linearization, which is accurate given our small errors (typically $< 0.1^\circ$); higher-order effects affect only the tails of the distribution, outside of measurable regions.

For the energy, the model predicts $\mu = \log \hat{E}$ and $\sigma_{\log E}^2$. Assuming $\log E \sim \mathcal{N}(\mu, \sigma_{\log E}^2)$, which is verified in the next section, the implied log-normal moments are

$$\mathbb{E}[E] = \exp\left(\mu + \frac{1}{2}\sigma_{\log E}^2\right), \quad (31)$$

$$\text{Var}(E) = (\exp(\sigma_{\log E}^2) - 1) \exp(2\mu + \sigma_{\log E}^2). \quad (32)$$

Reporting intervals in log-space (then exponentiating) preserves symmetry and calibration.

5.2. Calibration assessment

Uncertainty calibration is evaluated using two standard diagnostics.

First we inspect standardized residuals for all predicted quantities. For any target y with predictive mean \hat{y} and predictive

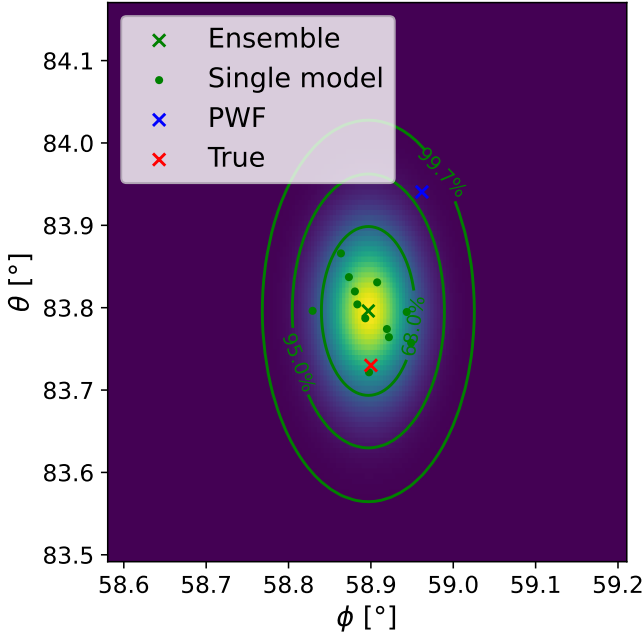


Figure 11: Direction reconstruction with uncertainty estimation. The individual models (green dots) predict a correction to the PWF direction (blue cross), their mean defines the deep ensemble prediction (green cross). The predicted covariance matrix gives the predicted uncertainty distribution which allows to create confidence intervals around the predicted value. Here the true value is inside the "1 σ " interval (68% isoline).

standard deviation $\hat{\sigma}_y$, the standardized residual is

$$z = \frac{y - \hat{y}}{\hat{\sigma}_y}. \quad (33)$$

Under a well-calibrated assumption, the residual should follow a standard Gaussian distribution. Figure 12 shows the empirical distributions of standardized residuals for reconstructed quantities θ , ϕ and $\log E$, assumed to be Gaussian given the loss function used and the previous section. They closely follow a standard normal, with only mild tail deviations.

Second, we inspect the coverage plot, which should follow the diagonal for a well-calibrated model. Figure 13 shows the coverage plots for θ , ϕ , and $\log E$. This plot is constructed by computing for each event the nominal coverage level $p = \text{erf}(|z|/\sqrt{2})$, which represents the probability that a standard normal variable falls within $\pm|z|$ of the mean. The empirical CDF of these coverage values is then plotted against the coverage level itself. If the predicted uncertainties are well-calibrated, this CDF should follow the diagonal, indicating that X% of events have standardized residuals within the X% confidence interval. If the curve lies above the diagonal, it indicates under-confidence (more than X% of events lie in the X% confidence intervals), while if it lies below, it indicates overconfidence (the model's uncertainty estimates are too small). The black envelope shows the expected behavior for standard normal variable, with 3σ confidence.

Here, all three are close to uniform, with only mild deviations. For the energy and zenith angle θ , the calibration is

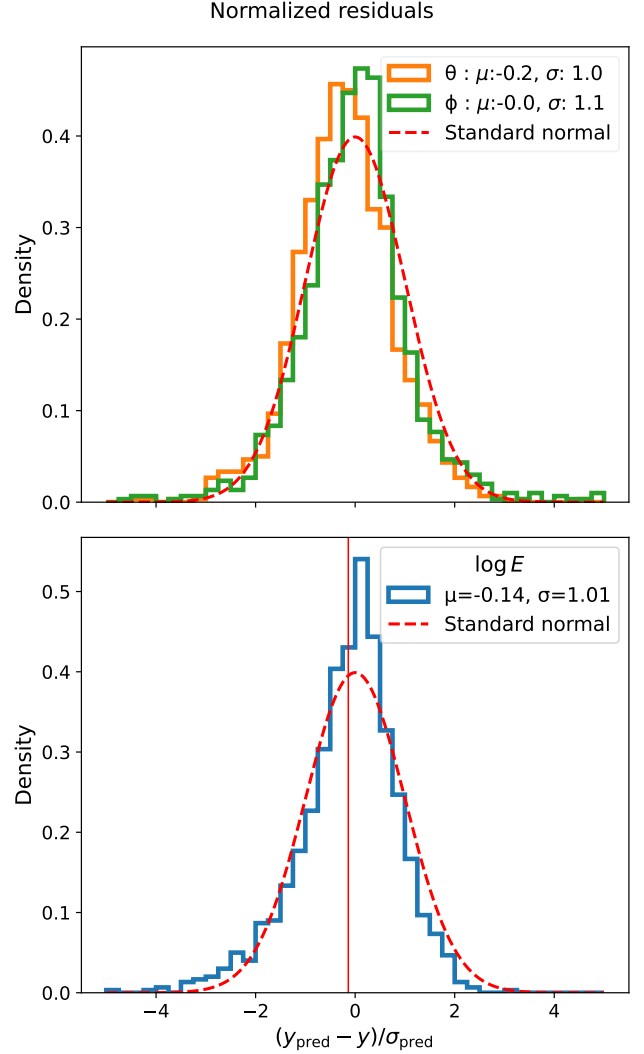


Figure 12: Standardized residuals for the three direction components (top: θ , ϕ) and for $\log E$ (bottom). The red curve is a standard Gaussian distribution $\mathcal{N}(0, 1)$. The close match supports the Gaussian assumption.

good at every level, with slight overconfidence at the tail (99.7% and above). For ϕ , the overconfidence at the tails is a more pronounced but good calibration at lower levels. Overall, the coverage plot indicates good calibration of the uncertainty estimates for all variables.

6. Robustness to setup variations

In this section, we evaluate the robustness of the trained models to variations in the experimental setup. This is crucial for real-world applications, where conditions may differ from those in the training simulations. We consider four main types of variations: increased noise levels, variation in antenna gain arising from miscalibration, changes in antenna positions, and variations in the number of available antennas.

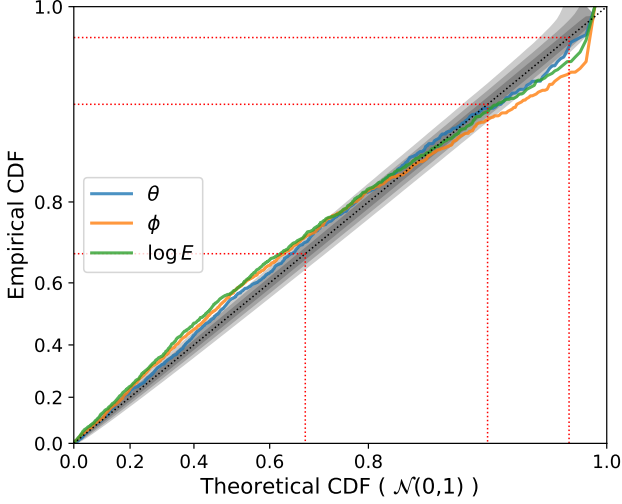


Figure 13: Coverage plot for zenith angle (orange), azimuth angle (green), and log electromagnetic energy (blue). The red dotted lines indicate 68%, 95%, and 99.7% quantiles for a standard normal distribution. The black dotted line is the coverage plot for a perfectly calibrated model. The shaded gray region corresponds to the expected behavior for standard Gaussian distributions. We see that the lines are close to the expected distribution, indicating good calibration despite some deviations.

6.1. Increased threshold levels

The networks have been trained on a set of events where every antenna that received a signal over $5\sigma_{\text{noise}}$ has been considered as triggered. In practice, the trigger algorithm is more complex in autonomous radio detection [25]. With this test, we try to capture the effect of a more conservative trigger threshold on the performances of the GNN. To model this, we evaluated the performances of pGNN models on a dataset with $5\sigma_{\text{noise}}$, $6\sigma_{\text{noise}}$, $7\sigma_{\text{noise}}$, $8\sigma_{\text{noise}}$, and $9\sigma_{\text{noise}}$ thresholds and looked at the evolution of the performances. With a $5\sigma_{\text{noise}}$ threshold, 1200 evaluation events are available for reconstruction. With a $9\sigma_{\text{noise}}$ threshold, only 867 events remain, as many events were left with not enough triggered DUs to perform reconstruction.

The results from this test are shown in Figure 14. The performances of the direction reconstruction methods suffer no degradation. One reason for this constant performance is that increasing the threshold has the same effect at antenna positions as lowering the amplitude, thus corresponding to the footprint a lower-energy event would have had at first order, thus fully reconstructible by the different reconstruction methods. This hypothesis is further confirmed by the energy reconstruction that underestimates the energy value while keeping the same resolution over the different threshold levels.

6.2. Variation in the number of available antennas

This robustness test is crucial in real-world scenarios where some antennas may be temporarily offline or malfunctioning. To simulate this, we create modified validation sets by randomly deactivating 5%, 10%, 20%, 30%, and 40% of the antennas. We remove successively more antennas from the complete layout and remove the corresponding antennas from every event. This procedure reflects realistic outage patterns where some events

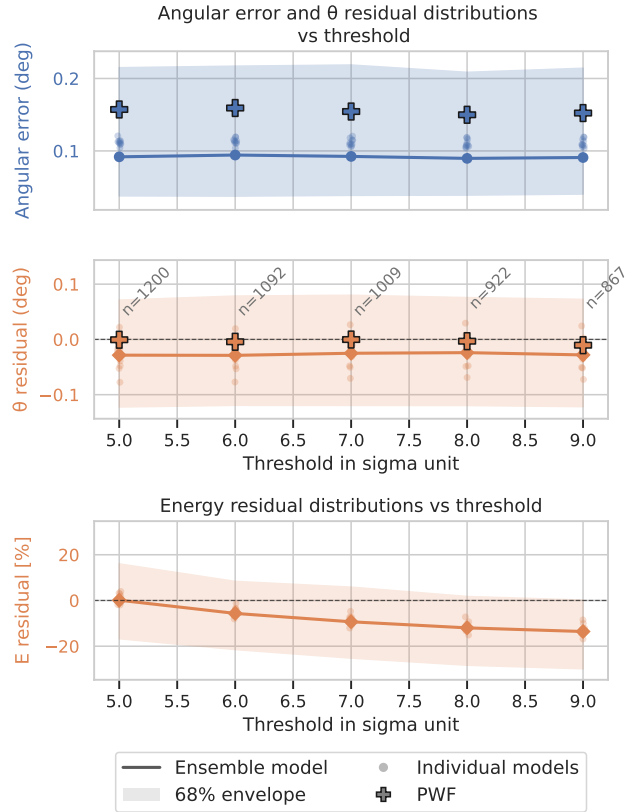


Figure 14: Top: Angular resolution (median values) and zenith angle bias (mean values) as a function of trigger threshold for the ensemble pGNN model (solid line), the PWF estimator (crosses) and single models (transparent dots). The angular resolution and error on θ stay stable. Bottom: Energy resolution as a function of the fraction of trigger threshold values for pGNN ensemble (solid line) and single models (transparent points). The energy resolution worsens from 16.4% to 23.0% with 40% antennas deactivated.

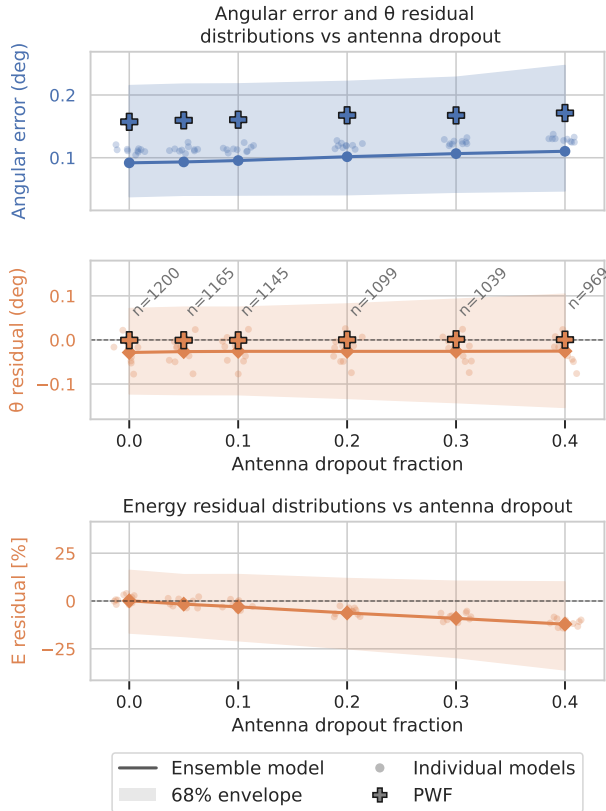


Figure 15: Angular resolution (median values) and zenith angle bias (mean values) as a function of the fraction of deactivated antennas for the ensemble pGNN model (solid line) and the PWF estimator (crosses) and single models (transparent dots). The angular resolution degrades from 0.09° to 0.11° with 40% antennas deactivated. Bottom: Energy resolution as a function of the fraction of deactivated antennas for the ensemble pGNN model. The energy resolution worsens from 16.4% to 23.0% with 40% antennas deactivated.

may not pass the trigger condition anymore, as fewer than 5 antennas may remain. 1200 events are available for testing with no antennas deactivated, and only 969 events remain when 40% of antennas are deactivated. The performance of the ensemble pGNN model, trained on the full set of antennas, is then evaluated on these modified datasets. As shown in Figure 15, the angular resolution degrades negligibly, increasing from 0.09° to 0.11° when 40% of antennas are deactivated. Moreover, no bias is introduced in the reconstruction of θ or ϕ , and the performances of the GNN models are systematically better than for the PWF, which suggests that the correction of the PWF is valid.

The energy resolution worsens more significantly, from 16.4% to 23.0%. Furthermore, a strong bias is noticeable as the antenna dropout fraction increases. Contrary to the previous test, where the resolution stayed constant but the prediction got bias, here the resolution degrades because these random antenna malfunctions do not imitate the footprint of a lower-energy event. Similar events have thus never been seen during training.

6.3. Antenna gain variation

To evaluate the effect of antenna gain variations, we simulate scenarios where the gain of each antenna is randomly altered. We multiply the transfer function $\mathcal{R}(v)$ from Eq. 4 by a Gaussian random factor with mean 1 and standard deviation of 0%, 5%, 10%, 15%, and 20%. The events used are the same 1200 events used for validation, the trigger is not recomputed at every new smearing value. This mimics realistic miscalibration effects that can occur in large arrays when we don't have the perfect calibration for every antenna. Contrary to other effects, this robustness test has partly been considered in the training set. Indeed, the smearing effect of 7% added to every amplitude before training is a way to model miscalibration in training.

The ensemble pGNN model trained on the training set with 7% smearing is then tested on these modified datasets. As shown in Figure 16, the angular resolution remains stable indicating no meaningful usage of the amplitude for inference by any of the pGNN models. The energy resolution shows a more noticeable degradation, worsening from 15.7% with no smearing to 24.4% with 20% smearing. We also see a large overestimation of the predicted energy of 13.9% at 20% smearing. This indicates that direction models are stable to amplitude variations but energy estimation is more sensitive to such changes, due to the strong correlation between shower energy and signal amplitude.

7. Conclusions, discussion

In this work, we applied deep ensemble graph neural networks to reconstruct cosmic ray direction and energy in GRAND like radio antenna array.

Using the geometry of the antenna array, physics-motivated features from voltage signals and prior knowledge of the direction, thanks to a plane-wavefront reconstruction, the ensemble pGNNs performs noticeably better on direction reconstruction (0.092°) than the usual plane-wavefront approach (0.16°) and on par with traditional physics based approach performed on electric field (ADF) on similar array geometries. For energy, the ensemble pGNN achieves a resolution of 16.4% for the electromagnetic component based on voltage signals. There are currently no established methods for a direct comparison for reconstruction on voltage signals, but the result is promising. Importantly, the model also provides uncertainty estimates that are well calibrated and are useful for downstream analyses.

We also checked how robust the networks are when the experimental conditions change—by changing triggering conditions, modifying antenna gains, or randomly removing antennas. The direction reconstruction is remarkably stable under these tests. Energy reconstruction shows a higher sensitivity to these variations, particularly in the presence of antenna dropouts, emphasizing the importance of incorporating a broader range of scenarios during training.

Taken together, these results show that deep ensemble GNNs are a strong candidate for improving cosmic-ray reconstruction with radio arrays. Future steps include adding more physics-driven features, extending the method to other detector layouts, and applying it to real data from existing observatories. The

combination of deep learning and domain knowledge has clear potential to push radio detection of cosmic rays further.

Acknowledgements

We thank the GRAND Collaboration for the discussion and useful insights for the simulations. We also thank the GRAND machine learning group (in particular C. Guépin, O. Macias, S. El Bouch and S. Prunet) for suggestions and discussions around the method. Simulations were performed using the computing resources at the IN2P3 Computing Centre (Villeurbanne, France), a partnership between CNRS/IN2P3 and CEA/DSM/Irfu.

References

- [1] HAWC Collaboration, The high-altitude water cherenkov (hawc) observatory in méxico: The primary detector, *Nucl. Instrum. Methods Phys. Res. A* 1052 (2023) 168253. doi:<https://doi.org/10.1016/j.nima.2023.168253>. URL <https://www.sciencedirect.com/science/article/pii/S0168900223002437>
- [2] S. Ohm, S. Wagner, Current status and operation of the h.e.s.s. array of imaging atmospheric cherenkov telescopes, *Nucl. Instrum. Methods Phys. Res. A* 1055 (2023) 168442. doi:<https://doi.org/10.1016/j.nima.2023.168442>. URL <https://www.sciencedirect.com/science/article/pii/S0168900223004321>
- [3] Pierre Auger Collaboration, The fluorescence detector of the pierre auger observatory, *Nucl. Instrum. Methods Phys. Res. A* 620 (2) (2010) 227–251. doi:<https://doi.org/10.1016/j.nima.2010.04.023>. URL <https://www.sciencedirect.com/science/article/pii/S0168900210008727>
- [4] Telescope Array Collaboration, Telescope array experiment, *Nuclear Physics B - Proceedings Supplements* 175-176 (2008) 221–226, proceedings of the XIV International Symposium on Very High Energy Cosmic Ray Interactions. doi:<https://doi.org/10.1016/j.nuclphysbps.2007.11.002>. URL <https://www.sciencedirect.com/science/article/pii/S0920563207007992>
- [5] D. Ardouin, et al., Radio-detection signature of high-energy cosmic rays by the codalema experiment, *Nucl. Instrum. Methods Phys. Res. A* 555 (1) (2005) 148–163. doi:<https://doi.org/10.1016/j.nima.2005.08.096>. URL <https://www.sciencedirect.com/science/article/pii/S0168900205017468>
- [6] D. Charrier, et al., Autonomous radio detection of air showers with the trend50 antenna array, *Astroparticle Physics* 110 (2019) 15–29. doi:[10.1016/j.astropartphys.2019.03.002](https://doi.org/10.1016/j.astropartphys.2019.03.002). URL <http://dx.doi.org/10.1016/j.astropartphys.2019.03.002>
- [7] F. D. Kahn, I. Lerche, Radiation from cosmic ray air showers, *Proceedings of the Royal Society of London. A. Mathematical and Physical Sciences* 289 (1417) (1966) 206–213. arXiv:<https://royalsocietypublishing.org/rspa/article-pdf/289/1417/206/55891/rspa.1966.0007.pdf>, doi:[10.1098/rspa.1966.0007](https://doi.org/10.1098/rspa.1966.0007). URL <https://doi.org/10.1098/rspa.1966.0007>
- [8] GRAND Collaboration, The giant radio array for neutrino detection (GRAND): Science and design, *Science China Physics, Mechanics and Astronomy* 63 (1) (aug 2019). doi:[10.1007/s11433-018-9385-7](https://doi.org/10.1007/s11433-018-9385-7). URL <https://doi.org/10.1007%2Fs11433-018-9385-7>
- [9] A. Castellina, Pierre Auger Collaboration, AugerPrime: the Pierre Auger Observatory Upgrade, in: *European Physical Journal Web of Conferences*, Vol. 210 of European Physical Journal Web of Conferences, 2019, p. 06002. arXiv:[1905.04472](https://arxiv.org/abs/1905.04472), doi:[10.1051/epjconf/201921006002](https://doi.org/10.1051/epjconf/201921006002).
- [10] A. Weltman, P. Bull, S. Camera, K. Kelley, H. Padmanabhan, J. Pritchard, A. Raccanelli, S. Riemer-Sørensen, L. Shao, S. Andrianomena, et al., Fundamental physics with the square kilometre array, *Publications of the*

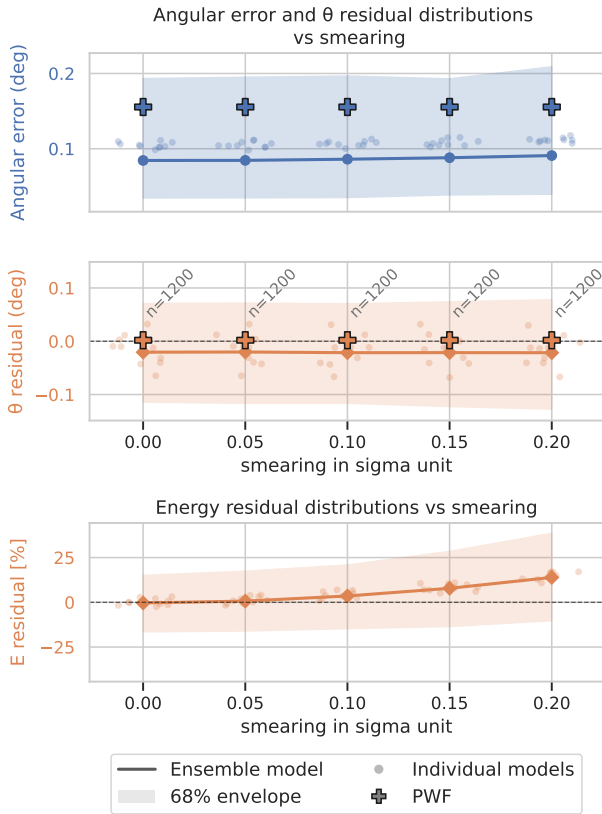


Figure 16: Angular resolution (median values) and zenith angle bias (mean values) as a function of miscalibration for the ensemble pGNN model (solid line) and the PWF estimator (crosses) and single models (transparent dots). The angular performances don’t improve. Bottom: Energy resolution as a function of the fraction of deactivated antennas for the ensemble pGNN model. The energy resolution worsens from 15.9% to 24.0% with 20% smearing on antenna amplitudes.

- Astronomical Society of Australia 37 (2020) e002. doi:10.1017/pasa.2019.42.
- [11] A. Ferrière, et al., Analytical planar wavefront reconstruction and error estimates for radio detection of extensive air showers, *Nucl. Instrum. Methods Phys. Res. A* 1072 (2025) 170178. doi:https://doi.org/10.1016/j.nima.2024.170178. URL https://www.sciencedirect.com/science/article/pii/S0168900224011045
- [12] A. Corstanje, et al., The shape of the radio wavefront of extensive air showers as measured with lofar, *Astroparticle Physics* 61 (2015) 22–31. doi:https://doi.org/10.1016/j.astropartphys.2014.06.001. URL https://www.sciencedirect.com/science/article/pii/S0927650514000851
- [13] M. Guelfand, et al., Reconstruction of inclined extensive air showers using radio signals: From arrival times and amplitudes to direction and energy, *Astroparticle Physics* 171 (2025) 103120. doi:https://doi.org/10.1016/j.astropartphys.2025.103120. URL https://www.sciencedirect.com/science/article/pii/S092765052500043X
- [14] L. Guelzow, et al., Modelling the Radio Emission of Inclined Air Showers in the 50-200 MHz Frequency Band for GRAND, *PoS ARENA2024* (2024) 063. doi:10.22323/1.470.0063.
- [15] A. Ferriere, et al., Reconstruction of cosmic-ray properties with uncertainty estimation using graph neural networks in GRAND, in: *Proceedings of 39th International Cosmic Ray Conference — PoS(ICRC2025)*, Vol. 501, 2025, p. 253. doi:10.22323/1.501.0253.
- [16] Y. Wang, et al., Dynamic graph cnn for learning on point clouds, *ACM Trans. Graph.* 38 (5) (2019). doi:10.1145/3326362. URL https://doi.org/10.1145/3326362
- [17] ICECUBE Collaboration, Graph Neural Networks for Low-Energy Event Classification & Reconstruction in IceCube, *Journal of Instrumentation* 17 (11) (2022) P11003, arXiv:2209.03042 [astro-ph, physics:hep-ex, physics:physics]. doi:10.1088/1748-0221/17/11/P11003. URL http://arxiv.org/abs/2209.03042
- [18] R. Garcia Ginez, Graph neural network model to classify between CR and gamma rays in ALPAQUITA (SD), *PoS ICRC2025* (2025) 653. doi:10.22323/1.501.0653.
- [19] P. Koundal, ICECUBE Collaboration, Machine learning driven reconstruction of cosmic-ray air showers for next generation radio arrays, *PoS ICRC2025* (2025) 309. doi:10.22323/1.501.0309.
- [20] O. Macias, et al., Simulation-Based Inference for Direction Reconstruction of Ultra-High-Energy Cosmic Rays with Radio Arrays (8 2025). arXiv:2508.15991. URL https://arxiv.org/abs/2508.15991
- [21] J. Alvarez-Muñiz, et al., Monte carlo simulations of radio pulses in atmospheric showers using zhaires, *Astroparticle Physics* 35 (6) (2012) 325–341. doi:10.1016/j.astropartphys.2011.10.005. URL http://dx.doi.org/10.1016/j.astropartphys.2011.10.005
- [22] A. Benoit-Lévy, et al., Pruning: a tool to optimize the layout of large scale arrays for ultra-high-energy air-shower detection, *Journal of Instrumentation* 19 (2024) P04006. doi:10.1088/1748-0221/19/04/P04006.
- [23] G. Burke, et al., The numerical electromagnetics code (nec) - a brief history, in: *IEEE Antennas and Propagation Society Symposium*, 2004., Vol. 3, 2004, pp. 2871–2874 Vol.3. doi:10.1109/APS.2004.1331976.
- [24] GRAND Collaboration, GRANDlib: A simulation pipeline for the Giant Radio Array for Neutrino Detection (GRAND), *Computer Physics Communications* 308 (2025) 109461. doi:https://doi.org/10.1016/j.cpc.2024.109461. URL https://www.sciencedirect.com/science/article/pii/S0010465524003849
- [25] GRAND Collaboration, Towards the giant radio array for neutrino detection (GRAND): the GRANDProto300 and GRAND@Auger prototypes, accepted for pub. in *JINST* (2025). arXiv:2509.21306. URL https://arxiv.org/abs/2509.21306
- [26] V. Decoene, et al., Radio wavefront of very inclined extensive air-showers: A simulation study for extended and sparse radio arrays, *Astroparticle Physics* 145 (2023) 102779. doi:10.1016/j.astropartphys.2022.102779. URL http://dx.doi.org/10.1016/j.astropartphys.2022.102779
- [27] O. Martineau-Huynh, The Giant Radio Array for Neutrino Detection - experimental status and plans, *PoS ICRC2025* (2025) 1114. doi:10.22323/1.501.1114.
- [28] E. Polisensky, Lfmap: A low frequency sky map generating program, *Long Wavelength Array Memo Series* 111 (2007) 515.
- [29] F. Scarselli, et al., The graph neural network model, *IEEE Transactions on Neural Networks* 20 (1) (2009) 61–80. doi:10.1109/TNN.2008.2005605.
- [30] D. Nix, A. Weigend, Estimating the mean and variance of the target probability distribution, in: *Proceedings of 1994 IEEE International Conference on Neural Networks (ICNN'94)*, Vol. 1, 1994, pp. 55–60 vol.1. doi:10.1109/ICNN.1994.374138.
- [31] S. Chiche, et al., Loss of coherence and change in emission physics for radio emission from very inclined cosmic-ray air showers, *Phys. Rev. Lett.* 132 (2024) 231001. doi:10.1103/PhysRevLett.132.231001. URL https://link.aps.org/doi/10.1103/PhysRevLett.132.231001

Appendix A. Influence of the training size on the reconstruction performances

For the training of the GNN models, we use up to 5000 realistic simulated events. In this appendix, we study the dependence of the reconstruction performance on the size of the training dataset. To this end, we train models using 300, 500, 1000, 2000, 3000, 4000, and 5000 training events. For each dataset size, we train 10 independent models and evaluate the performance of both the individual models and their ensemble. This procedure is applied to both pGNN and rGNN architectures. All other training hyper-parameters and model architectures are kept identical across dataset sizes. The validation set used is the same across the whole experiment.

Figures A.17 and A.18 show the evolution of the energy resolution and angular resolution, respectively, as defined in Section 4.

For the energy reconstruction, we observe an approximately linear relation between the resolution and the log of the training set size, suggesting further performance gains for larger training datasets. We also find that the inclusion of the PWF-based features does not significantly affect the energy reconstruction performance.

For direction reconstruction, models incorporating PWF-based inputs show a clear improvement over the rGNN models. We further observe that the performance of the pGNN models stops improving for training set sizes above approximately 2000 events, whereas the rGNN models continue to improve up to 5000 training events. This behavior supports the use of PWF cartesian coordinates as inputs to GNNs for direction reconstruction when the size of the training set is limited. The reported trends are robust across different random initializations, as quantified by the spread among the individual models in each ensemble.

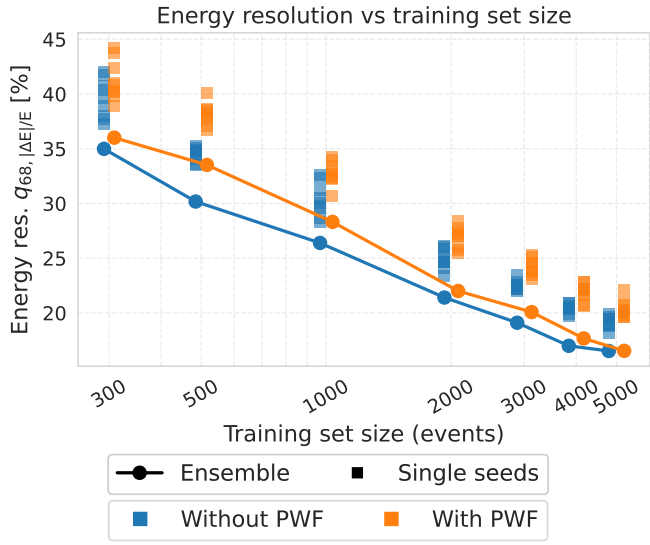


Figure A.17: Energy resolution as a function of training set size. Ensemble predictions (circles) and individual seed predictions (squares) are shown for models trained with (orange) and without (blue) PWF input. Energy resolution is defined as the 68% quantile on energy relative error $q_{68,|\Delta E|/E}$.

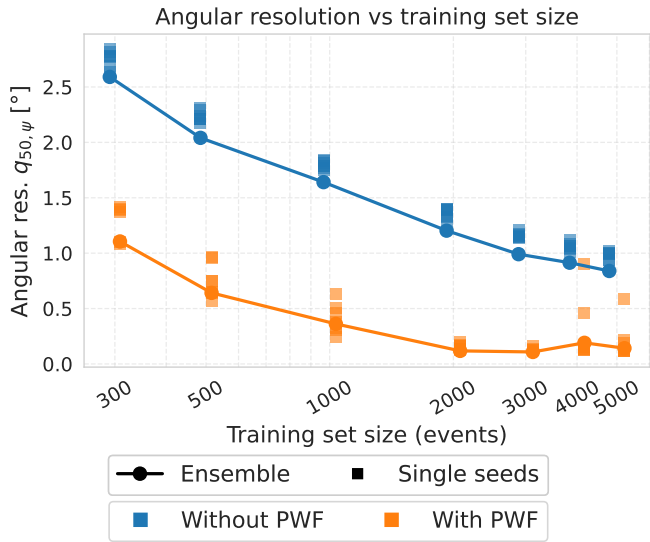


Figure A.18: Angular resolution as a function of training set size for direction reconstruction. Ensemble predictions (circles) and individual seed predictions (squares) are shown for models trained with (orange) and without (blue) point spread function (PSF) corrections. Angular resolution is defined as the median angular error $q_{50,\psi}$ in degrees.